

Micro-mechanical analysis of high modulus asphalt concrete pavement

Chundi Si^{a,b}, Xiaodong Zhou^{b,*}, Zhanping You^b, Ying He^a, Enli Chen^a, Ran Zhang^{c,b}

^a Institute of Transportation Environment and Safety Engineering, Shijiazhuang Tiedao University, Shijiazhuang, Hebei 050043, China

^b Department of Civil and Environmental Engineering, Michigan Technological University, Houghton, MI 49931, USA

^c School of Highway, Chang'an University, South Erhuan Middle Section, Xi'an, Shaanxi 710064, China

HIGHLIGHTS

- The micro-parameters of DEM were determined based on the uniaxial compression test.
- DEM of HMAC pavement was established and applied at static loading conditions.
- The displacement, vertical & horizontal stress and shear stress of HMAC were studied.
- HMAC layer improved stress distribution state and resistance to deformation.

ARTICLE INFO

Article history:

Received 17 November 2018

Received in revised form 10 April 2019

Accepted 3 June 2019

Available online 8 June 2019

Keywords:

Asphalt pavement

Micro-mechanical analysis

Discrete Element Method (DEM)

High Modulus Asphalt Concrete (HMAC)

ABSTRACT

The objective of this study is to investigate the micro-mechanical characteristics of High Modulus Asphalt Concrete (HMAC) pavement structure under loads. The Discrete Element Method (DEM) was employed in this study to build the models for HMAC pavement and conventional asphalt pavement structures. The laboratory tests and DEM simulations of uniaxial compression tests were conducted on the materials of HMAC pavement structure layers. To simulate the mechanical behavior of the asphalt mixture, micro-parameters were adjusted to fit with the strain–stress curve results from lab-test. The displacement and stress distribution in vertical and horizontal directions, and the shear stress in the horizontal direction were analyzed for the HMAC pavement and conventional asphalt pavement. The results showed that the maximum vertical displacement of HMAC pavement (0.25–0.293 mm) was less than that of the conventional asphalt pavement (0.3–0.324 mm). The application of HMAC decreased the vertical stress in all structural layers except the upper surface layer. The HMAC decreased the horizontal stress in the sub-base layer. Though the HMAC pavement had a slightly greater horizontal shear stress in the upper and middle surface layers than the conventional asphalt pavement, its shear resistance was. Therefore, the results indicated HMAC layer can enhance the resistance to deformation and reduce the rutting potential in asphalt pavement.

Published by Elsevier Ltd.

1. Introduction

High-modulus asphalt concrete (HMAC) was originated from France in 1980s to increase the rutting mitigation resistance and the stiffness of asphalt base layers [1]. Generally, there are three methods to obtain high modulus binders which contribute the most of the higher stiffness of HMAC: use hard-grade asphalt binders that have low penetration and high softening points [2]; use polymer modifier, such as SBS and lake asphalt [3–5]; use high-modulus agent [3,6,7]. HMAC shows evident higher stiffness when compared with conventional asphalt concrete. Pavements with HMAC base layers were reported to have good resistance to

rutting and fatigue with the context of climate in France [7]. By applying HMAC, the thickness of the base layer can be greatly reduced while the performance remains the same. However, researchers still have great concerns on the mechanical performance of the HMAC in more inclement climate condition, especially its low temperature performance. Researchers from Spain carried out the repetitive loading axial tests at high temperature (40–45 °C) and found the permanent deformation resistance of HMAC was highly related with the asphalt grade and voids contents [2,7]. According to H.J. Lee et al. the HMAC test section had lower bottom tensile strain than conventional AC in full-scale tests, despite the thickness of HMAC was thinner than conventional AC [5]. As a result, the rutting depth occurred in the HMAC test section was half of that in the conventional AC, while the fatigue endurance limit of HMAC was within the fatigue criterion. Dawid Rys

* Corresponding author.

E-mail address: xzhou3@mtu.edu (X. Zhou).

et al. analyzed the low temperature performance on the HMAC in Poland and reported that the HMAC base layer pavements had 2.45 times cracking odds than conventional AC base layer pavements [8]. Lower voids contents (2–4%), lower stiffness modulus, softer asphalt binder of HMAC were recommended based on the France standards (voids contents up to 6%) when applied to cold weather. Researchers also investigated the feasibility of mix high-content of reclaimed asphalt pavement (RAP) in the HMAC, for the asphalt binder in RAP have hard grade because of volatilization and oxidation. Mechanical properties of HMAC with 0%, 15%, 30% and 50% RAP of were compared by Rodrigo Miró et al. by using laboratory tests including: stiffness modulus, toughness, moisture sensitivity, rutting and fatigue resistance [9]. Results shown the HMAC with high-content of RAP could have similar mechanical properties to conventional HMAC. T. Ma et al. employed wheel tracking test, bending beam test, moisture stability test, and fatigue resistance test to evaluate the performance of HMAC with RAP up to 50% percent [7]. As the tests results indicated, the dynamic modulus and failure strain were significantly decreased when RAP content reach to 40%. Additionally, the dynamic stability and tensile strength ratio also decreased tremendously with 50% RAP content.

Despite the successful application of HMAC in asphalt pavement, few studies were focused on the mechanical analysis of HMAC pavement in structure perspective. Finite element method (FEM) was used by M. Zheng et al. to simulate and predict the permanent deformation and fatigue life of HMAC pavement [10,11]. A preliminary rutting equation and an established fatigue equation were proposed and validated in those studies. However, in the FEM analysis, the elastic layer system is generally used to establish the pavement mechanics model, which assumes the materials of each layer are homogeneous, elastic, isotropic and interlayer continuous. In fact, these assumptions are not consistent with the granular, viscoelastic and anisotropic characteristics of the asphalt pavement. In addition, the micro-structure characteristics of the asphalt mixture is also not considered. Scholars also applied CCD digital photography, X-ray CT or high precision scanning to obtain and process digital images of the internal structure of the asphalt mixture and study its microstructure properties [12–14]. The microstructure characteristics of asphalt mixture were analyzed by the experimental method or through importing the digital information into the software of numerical simulation [15–17]. Thought image-analysis technology has greatly contributed to the internal structure analysis of asphalt mixture, it can't make insight investigation into the mechanical analysis of asphalt pavement structures.

Discrete Element Method (DEM) was used by researchers to investigate the mechanical performance of and failure mechanism of asphalt mixtures for its unique ability in simulating the discreteness of material. Chang and Meegoda [18] simulated viscoelastic properties of a hot mix asphalt mixture by the DEM and conventional tri-axial tests of an asphalt under different load conditions. You et al. [19,20] established a micro-structure model of aggregate-mortar-gap by the DEM and simulated the stiffness and complex modulus of the cylindrical asphalt mixture specimens and the asphalt mortar specimens. The simulation results agreed with the test results. Kim and Buttlar [21] established a micro-mechanical damage model of an asphalt mixture by the DEM and analyzed the crack characteristics of asphalt concrete. The bilinear cohesive force model was verified by the double cantilever beam, and the results of numerical simulation were aligned with the test results. Abbas et al. [22] simulated the micro-mechanical properties of SMA and asphalt mixture by the DEM. The numerical simulation results and experimental results were compared and analyzed. The viscoelastic response of asphalt mixture at high temperature and the principle of cracking at low temperature were

studied. Chen et al. [23] simulated the compaction process of asphalt mixture by the DEM and verified the simulation results with laboratory tests. Based on the verified models the gyratory compaction, vibration compaction and kneading compaction process were compared. Liu et al. [24] simulated the real particle shapes of the aggregate in the mixture by combining the MATLAB image processing method with the PFC5.0 FISH code and verified the efficiency and accuracy of the method. Using the real particle shapes, the Surperpave gyratory compaction model was established and specimens with different aggregates shapes were tested [25,26]. The results from laboratory and simulation shown that the flat and elongated aggregates decrease the compatibility of asphalt mixture.

Although 3D models are more realistic in many ways, they require huge amount of calculation ability to support the simulation. Especially when the study is focused on full-scale pavement structures, which could lead to millions of elements in 3D models. Also, as pointed by the former studies [27,28], 2D models could show the same influence trend as the 3D models. Besides, 2D models have advantages in describing the stress/strain and displacement development, while the 3D models must use more complex and indirect algorithm to transit. Therefore, 2D DEM was adopted in this study.

For the fast travel traffic loads, the loads application duration was short. Since the application duration is short and this study assumed the pavement was under a general climate situation which indicated the temperature was not too high, the asphalt mixtures should behavior more “elastic”. In other studies, the asphalt mixtures were applied to repeated loading for a relatively longer duration, under this situation the viscoelastic models would no doubt to be the best contact models [29,30]. In these studies, the assumption was the viscoelastic was the dominate performance. This study focused more on the stress/strain and displacement of the pavement structures, and there could be tiny cracks developed under the external loads. Therefore, the linear parallel bond contact model is suitable to describe the mechanical behavior of pavement structures under the above assumptions [31,32]. Therefore, to explore the mechanical response of HMAC pavement structure, 2D DEM and parallel bond contact model were employed by this study.

2. Determination of micro-parameters

The pavement structure model was established based on the test section of a highway in Hebei Province, China. The pavement structure included 5 layers from top to bottom: 4 cm asphalt concrete layer AC-13, 6 cm high modulus asphalt concrete layer HMAC-20, 8 cm asphalt treated base layer ATB-25, 35 cm cement treated base and 27 cm cement treated subbase (see Fig. 1).

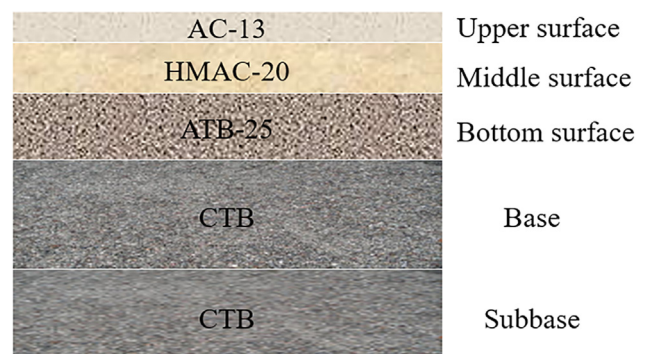


Fig. 1. HMAC pavement structure.

2.1. Experimental material

The two-dimensional discrete element specimen of each pavement structure material was generated, and the aggregate gradation of each structure layer is shown in Tables 1–4. According to the Chinese test regulations of asphalt and asphalt mixture for highway engineering (JTG E20-2011), the size of the discrete element specimen is 150 mm tall × 100 mm in diameter in uniaxial compression tests.

The upper surface layer selected dense graded asphalt concrete AC-13, in which SBS modified asphalt was used. The air void content of the asphalt concrete was 6.7%, and its gradation is shown in Table 1.

The HMAC-20 and 20# matrix asphalt were used in the middle surface layer. The air void content of the asphalt concrete was 3.9%, and its gradation is shown in Table 2.

The asphalt treated base ATB-25 with 70# matrix asphalt were applied in the bottom surface layer. The air void content of the asphalt concrete was 4.3%, and the gradation of asphalt treated base is shown in Table 3.

The base and subbase layers adopted cement stabilized gravel (including gravel, stone chips, and cement). Aggregate was limestone, cement content was 4%, and the gradation of cement treated base and subbase is shown in Table 4.

2.2. Establish of virtual uniaxial compression models

The virtual specimens were developed by random generation. The particles were generated with overlap according the mixture design in a rectangular container. The four walls of the rectangular container were fixed at the first stage of specimen's generation. The particles would re-arrange their position to reach equilibrium status. The walls could slightly move to release the stress inside the specimens. When both the average internal stress was around zero and the unbalance stress was smaller than 1×10^{-4} of the average internal stress, the specimens reached equilibrium status. Then the side walls of the container were deleted, and the linear parallel bond contact model was assigned to the specimen.

Table 1
Gradation of AC-13.

Sieve size (mm)	16.0	13.2	9.5	4.75	2.36	1.18	0.6	0.3	0.15	0.075
Rate of passing (%)	100	97.5	78.5	49.0	33.0	24.0	17.0	12.5	9.5	6.0

Table 2
Gradation of HMAC-20.

Sieve size (mm)	26.5	19.0	16.0	13.2	9.5	4.75	2.36	1.18	0.6	0.3	0.15	0.075
Rate of passing (%)	100	97.5	86.0	74.0	64.0	44.0	30.0	20.5	15.0	11.0	8.0	6.0

Table 3
Gradation of ATB-25.

Sieve size (mm)	31.5	26.5	19.0	16.0	13.2	9.5	4.75	2.36	1.18	0.6	0.3	0.15	0.075
Rate of Passing (%)	100	97.5	82.5	74.0	65.0	54.0	39.0	28.0	18.5	15.0	10.5	7.5	5.0

Table 4
Gradation of cement stabilized gravel.

Sieve size (mm)	31.5	19.0	9.5	4.75	2.36	0.6	0.075
Rate of passing (%)	100	81.2	56.2	40.6	25.1	10.6	5.2

2.3. Selection of micro-parameters

The mixture of fine aggregate and asphalt was defined as asphalt mortar, and only particles with the size of 2.36 mm or larger were considered in the DEM models to balance the calculation efficiency [33,34]. The parallel bond model was adopted when defining the contact mode among particles, and its constitutive model is shown in Fig. 2.

In the parallel bond constitutive model, g_s represents parallel bond radius; k_n and k_s represent the normal and tangential stiffness of the particles, respectively; \bar{k}_n and \bar{k}_s represent the normal and tangential stiffness of the parallel bond model, respectively; $\bar{\sigma}_c$ represents the normal strength of parallel bonding; $\bar{\sigma}$ represents cohesion; $\bar{\phi}$ represents the internal friction angle; μ represents the friction coefficient.

The relationship between micro-parameters and macro-parameters is established through deformation and strength. Normal stiffness and tangential stiffness are based on contact deformation (effective modulus E^* and stiffness ratio k^* in the deformability method). The relationship between effective modulus E^* and stiffness is shown in Eqs. (1) and (2).

The Deformability Method:

$$k_n = \frac{AE^*}{L}; k_s = \frac{k_n}{k^*} \quad (1)$$

$$\text{In equation: } A = \begin{cases} 2rt \cdot 2D(t=1) \\ \pi r^2 \cdot 3D \end{cases}; r = \begin{cases} \min(R^{(1)}, R^{(2)}) & \text{ball-ball} \\ R^{(1)} & \text{ball-facet} \end{cases};$$

The Pb-deformability Method:

$$\bar{k}_n = \frac{\bar{E}^*}{L}; \bar{k}_s = \frac{\bar{k}_n}{k^*} \quad (2)$$

$$\text{In equation: } r = \begin{cases} R^{(1)} + R^{(2)} & \text{ball-ball} \\ R^{(1)} & \text{ball-facet} \end{cases}$$

The micro-mechanical parameters used in this study were determined by a designed trial and error method. The micro-mechanical parameters in DEM were adjusted one by one to fit

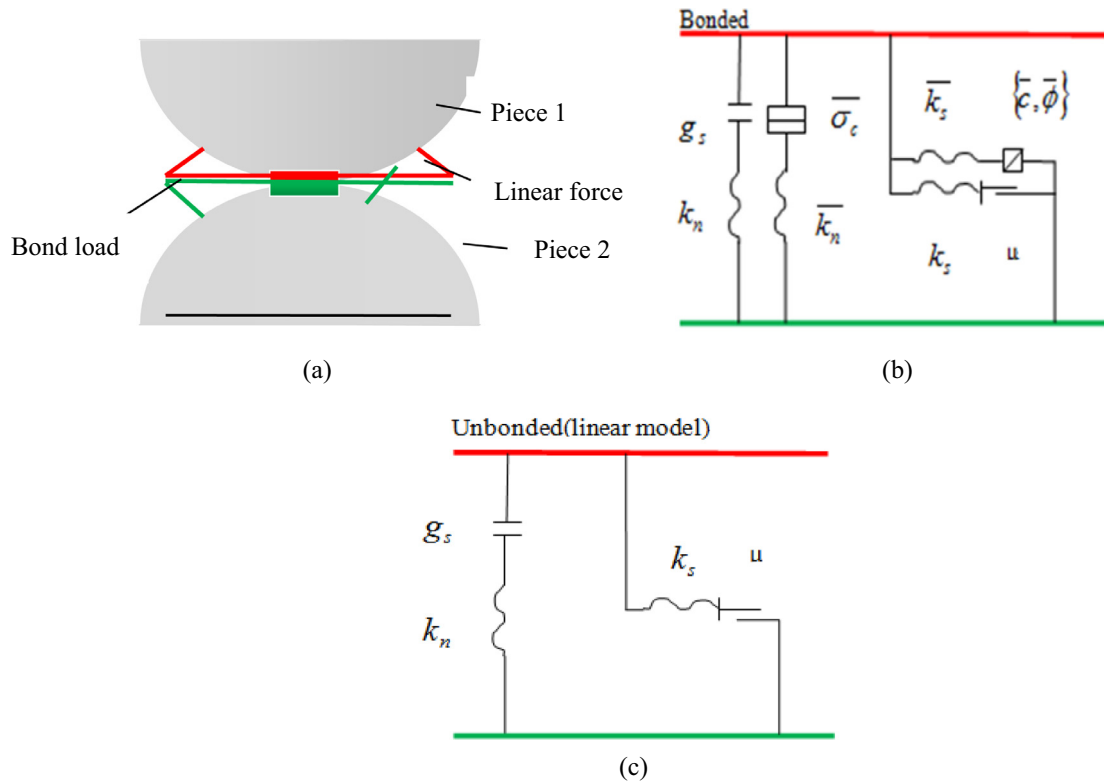


Fig. 2. A schematic diagram of a parallel bond constitutive model.

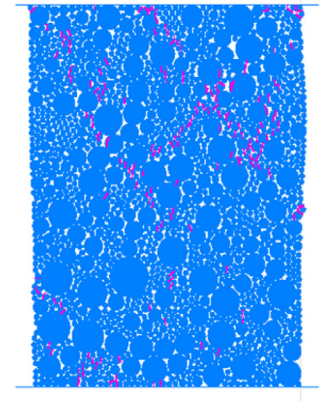
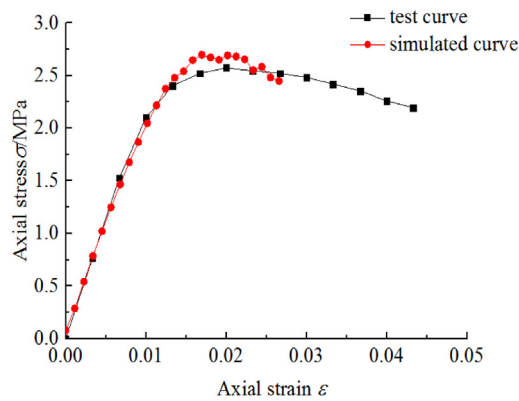
with the results of the uniaxial compression tests in the lab. As shown on Figs. 3–6, the axial stress of asphalt mixture specimens increased linearly with the axial strain before reaching the peak values which indicate the destruction of the specimens. In DEM models, the linear modulus of specimens is primarily controlled by the linear modulus (*emod*). Therefore, the *emod* was first determined by fitting with the lab test results. With a similar process, the bond strength (*pb_ten*) that is primarily related with the destruction strength was determined. The bond modulus (*pb_emod*) and friction coefficient (*fric*) were determined by the proliferation of cracks and the destruction behavior of specimens. The comparison of numerical simulation curves and experimental curves of structural layers are shown in Figs. 3–6.

The micro-parameters of the material for all pavement structure layers are shown in Table 5.

3. Simulation of HMAC pavement and conventional asphalt pavement under static load

3.1. Model establishment

Two-dimensional pavement structure DEM models of conventional asphalt pavement and HMAC pavement were established. The length was 2 m, and the depth was 0.8 m. The structure layers of the HMAC pavement were the same as those of conventional asphalt pavement except the middle surface layer. In conventional



(a) Test and simulated curves (b) Uniaxial compression specimen (c) Discrete element specimen

Fig. 3. Comparison between the test curve and the simulated curve of AC-13.

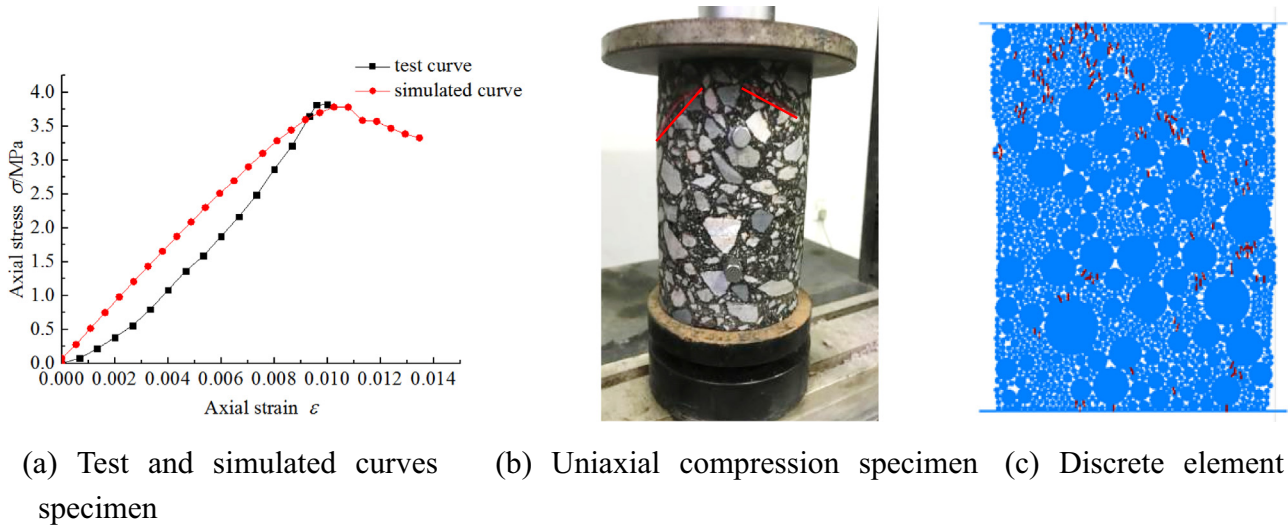


Fig. 4. Comparison between the test curve and the simulated curve of HMAC-20.

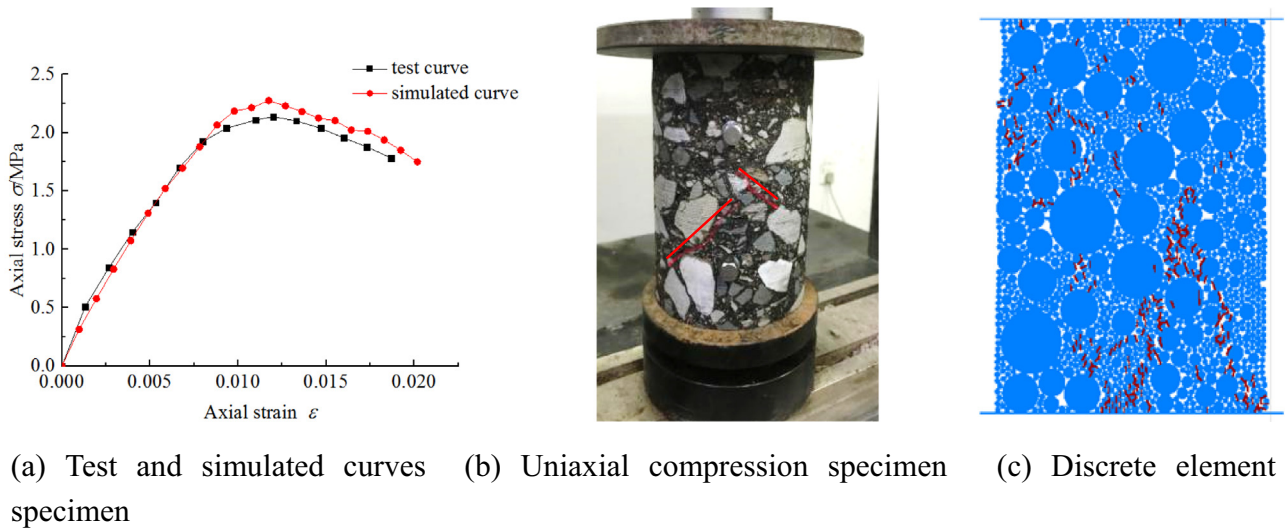


Fig. 5. Comparison between the test curve and the simulated curve of ATB-25.

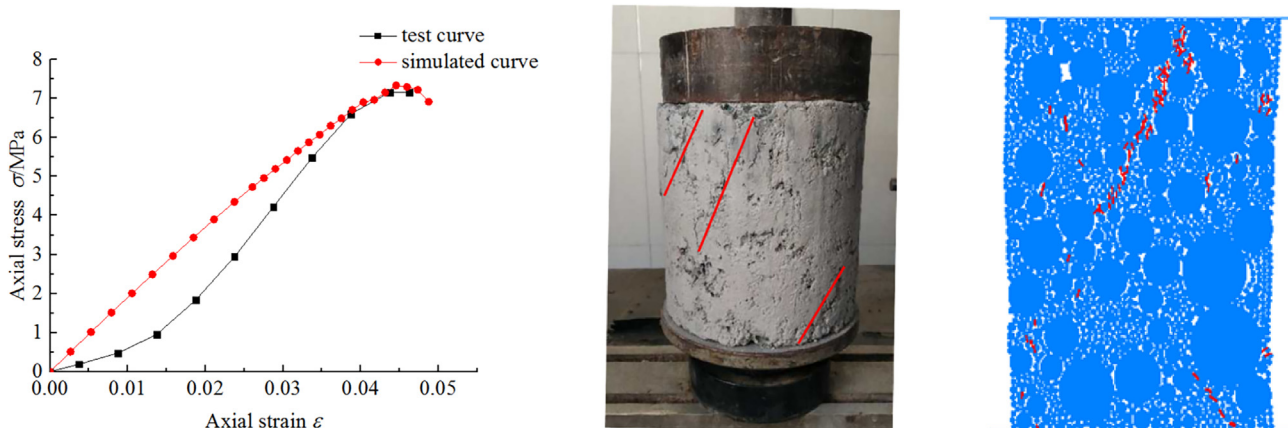


Fig. 6. Comparison between the test curve and the simulated curve of cement stabilized gravel.

Table 5

The micro-parameters of the material in each pavement structure.

Pavement structure layer	Linear modulus e_{mod} (Pa)	Bond modulus $pb_{e_{mod}}$ (Pa)	Bond strength pb_{ten} (Pa)	Friction coefficient $fric$
Upper surface layer (AC-13)	1.4×10^9	1.45×10^7	2.4×10^6	0.2
Middle surface layer (HMAC-20)	1.7×10^9	1.4×10^7	2.25×10^6	0.35
Bottom surface layer (ATB-25)	1.6×10^9	1.2×10^7	1.5×10^6	0.2
Base layer	2.5×10^8	2.3×10^7	4.8×10^6	0.5
Subbase layer	2.5×10^8	2.3×10^7	4.8×10^6	0.5

asphalt pavement, the middle surface layer used the same material as the upper surface layer, while in HMAC pavement the middle surface layer contains HMAC. The single axle with double wheel load was applied with the contact pressure of 0.7 MPa, and the distance between two tires was 10.65 cm. The wheel was represented by the circle with an equivalent circle diameter of 21.3 cm. The model was generated to satisfy the air void content requirement. To achieve the equilibrium state, the unbalanced stress in the model system was reduced to less than the average stress by 1×10^{-4} through the cycle calculation. Particles were generated according to the gradation information of the pavement structure layers. The application duration of the static loads was 0.03 s.

Models before loading for HMAC pavement are shown in Fig. 7 and Fig. 8.

Before loading, the contact force between particles increases from top to bottom, which was consistent with the pattern variations of geostatic pressure. The contact force was pressure, and no tension. After loading, the contact force among particles is shown below in Fig. 9.

After loading, the contact force among particles was concentrated, mainly distributed under the action of the wheels. The thicker the lines, the greater the contact-force. With increasing pavement depth, the load transfer was weakened gradually, and the contact force became smaller.

3.2. Vertical and horizontal displacement

The comparison in vertical displacement and horizontal displacement of the two pavement structures after static loading is shown in Figs. 10–11, respectively. The boundaries between the pavement structure layers were added after calculation to clearly show the stress distribution of each layer.

As shown in Fig. 10, maximum vertical displacement of road surface occurred in the center of the wheel load. The displacements of HMAC pavement and conventional asphalt pavement were 0.25–0.293 mm and 0.3–0.324 mm, respectively. Vertical displacement was symmetrical and decreased with the increasing pavement depth.

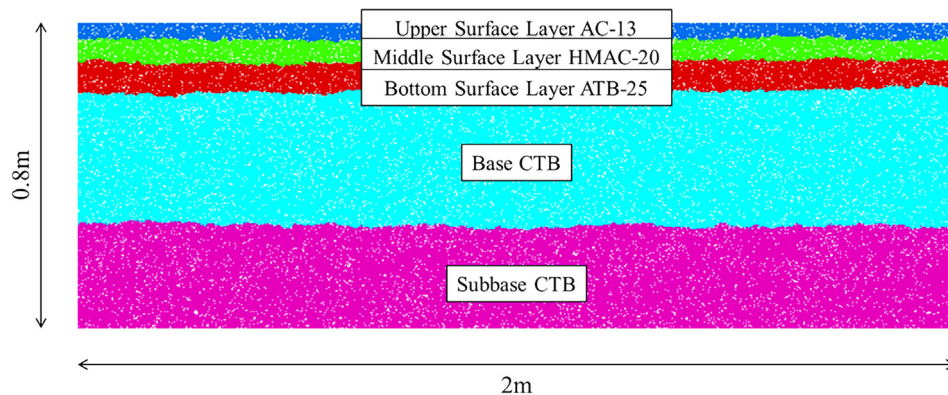


Fig. 7. The pavement structure model in equilibrium state before loading (upper surface layer, middle surface layer, bottom surface layer, base layer and subbase layer from top to bottom).

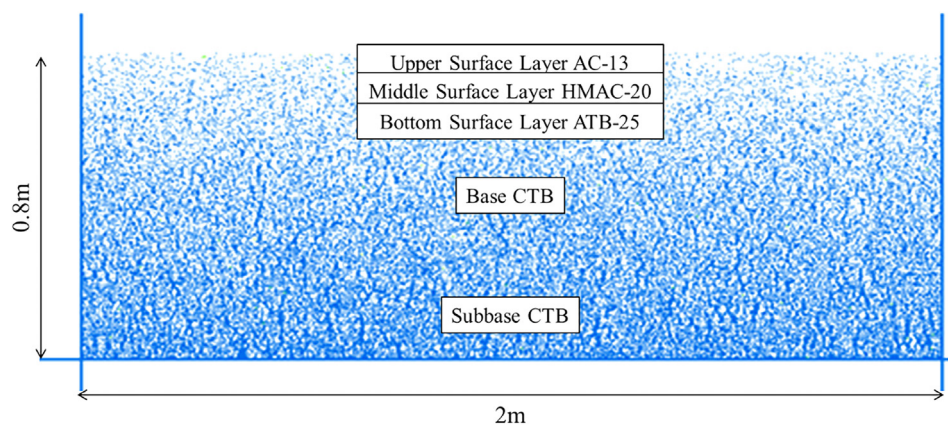


Fig. 8. Contact force distribution of pavement structure model in equilibrium before loading.

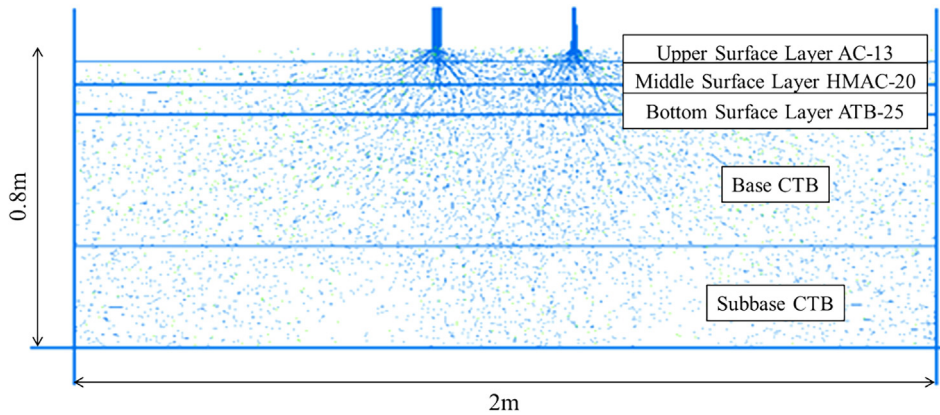


Fig. 9. The contact force distribution after double circular static loading.

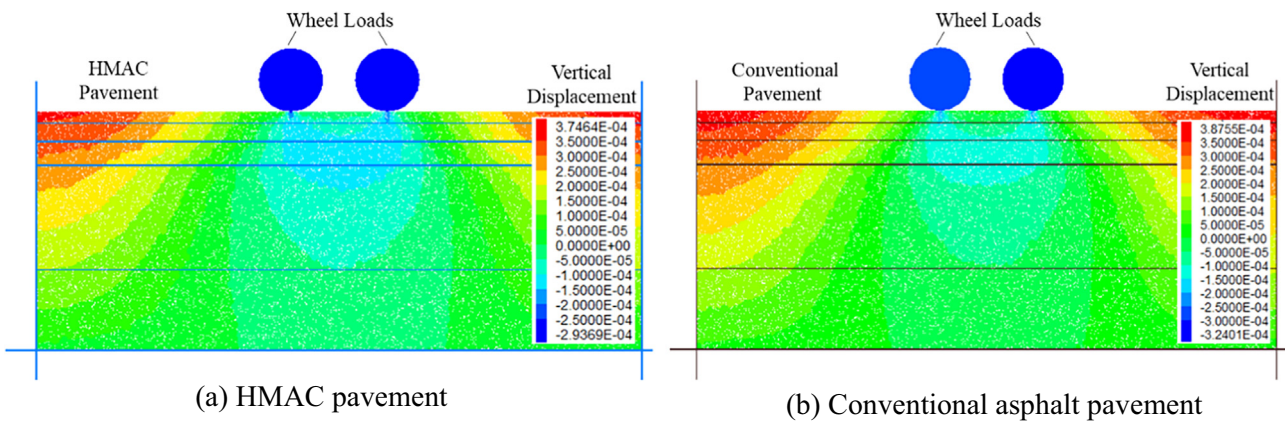


Fig. 10. Vertical displacement distribution after dual wheel static loading.

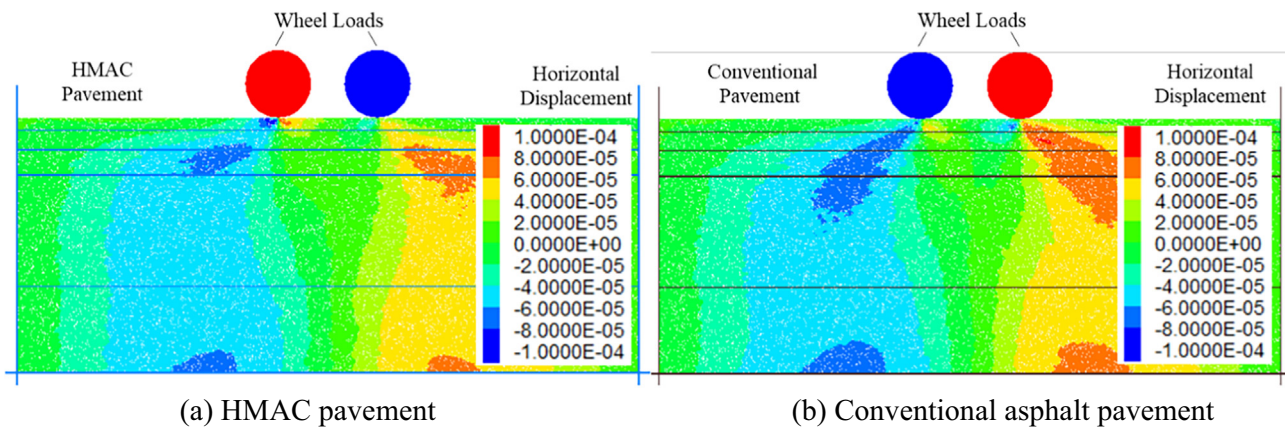


Fig. 11. Horizontal displacement distribution after dual wheel static loading.

As shown in Fig. 11, it could be concluded that the horizontal displacement at the bottom surface layer was large and symmetrical under the load of the left and right wheels. Compared to the HMAC pavement, the area over which horizontal displacement occurred within the conventional asphalt pavement was more extensive, which indicated that the high modulus layer can effectively restrain the movement of the particles in the horizontal direction.

3.3. Vertical and horizontal stress

The origin of X-Y coordinate system was placed at the centroid of the model. Because of the symmetry about X-axis, only the left side of the wheel was studied. Under the center of the wheel load ($x = -0.15975$ m), the following measurement circles were placed: a measurement circle with a radius of 2 cm at a depth of 4 cm; one with a radius of 4 cm at a depth of 10 cm; one with a radius of 4 cm

at a depth of 18 cm; one with a radius of 5.325 cm at a depth of 53 cm; one with a radius of 5 cm at a depth of 75 cm. From top to bottom, the measurement circles were numbered as 1–5, and there were 5 measurement circles in total.

The layout of the measurement circles is shown in Fig. 12.

The stress change records of the tests (called as **history** in the following) were obtained by the measurement circles (called as **measure** in the following). The **measure** at different locations recorded the horizontal stress (XX) and the vertical compressive stress (YY). The corresponding relationship between **measure** ID and **history** ID is shown in Table 6.

3.3.1. Vertical stress distribution

Under the static load, the horizontal and vertical stresses of the two types of asphalt pavement structures were calculated using the measurement circles. The comparison of vertical stress between the two types of asphalt pavement structures at different

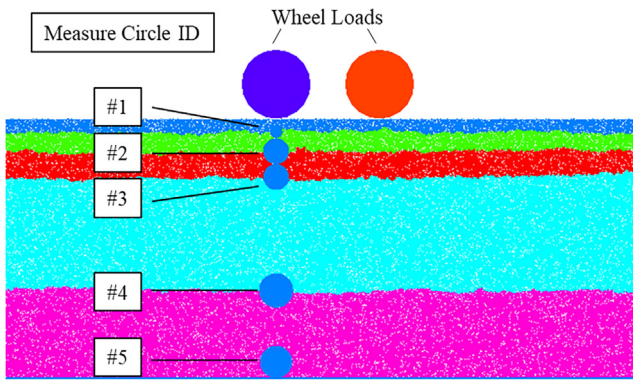


Fig. 12. The layout of the measurement circles for the bottom of each layer.

Table 6 The corresponding relationship between measure ID and history ID.

Measure ID		1	2	3	4	5
History ID	Horizontal stress (XX)	1	3	5	7	9
	Vertical stress (YY)	2	4	6	8	10

depths beneath the left wheel load center is shown in Fig. 13 and Table 7.

As shown in Fig. 13 and Table 7, for the two types of asphalt pavement structure, the vertical stress at different depths gradually decreased with increasing depth, and the rate of change was greater in the surface layers. The maximum pressure stress appeared in the upper surface layer.

In comparison to the conventional asphalt pavement, the HMAC pavement had a smaller vertical stress in the middle surface layer since it is a high modulus layer. However, the vertical stress of the upper surface layer of the HMAC pavement was greater than that of the ordinary asphalt pavement. The vertical stress of the bottom surface layer, base layer and subbase layer of the HMAC pavement was smaller compared to the conventional asphalt pavement. These results are consistent with previous studies [22,23].

3.3.2. Horizontal stress distribution

The comparison of horizontal stress between the two types of asphalt pavement structures at different depths beneath the left wheel load center is shown in Fig. 14 and Table 8.

As shown in Fig. 14 and Table 8, the horizontal stress tended to gradually decrease with increasing depth, and it became tensile stress at a certain depth. The maximum horizontal compressive stress appeared in the upper surface layer of both the HMAC and conventional asphalt pavement, and the maximum tensile stress occurred in the subbase layer of both pavements. Moreover, the tensile stress in the HMAC pavement was consistently smaller than that of the conventional asphalt pavement. These results showed that the high modulus layer could effectively reduce the tensile stress of pavement structure and improve the flexural ability of the pavement.

In order to accurately monitor the horizontal tensile stress distribution in the bottom surface layer, base layer and subbase layer, measurement circles with varied radii were placed at various horizontal locations and depths. The horizontal coordinates included the outer edge of the wheel ($x = -0.26625$ m), the center of the wheel load ($x = -0.15975$ m), the inner edge of the wheel ($x = -0.05325$ m), and the center of the wheel gap ($x = 0.0$ m). For the bottom surface layer, measurement circles with a radius of 2 cm were horizontally arranged at depths of 12 cm and 16 cm. For the base layer, measurement circles with a radius of 3.5 cm were arranged horizontally at depths of 21.5 cm, 28.5 cm,

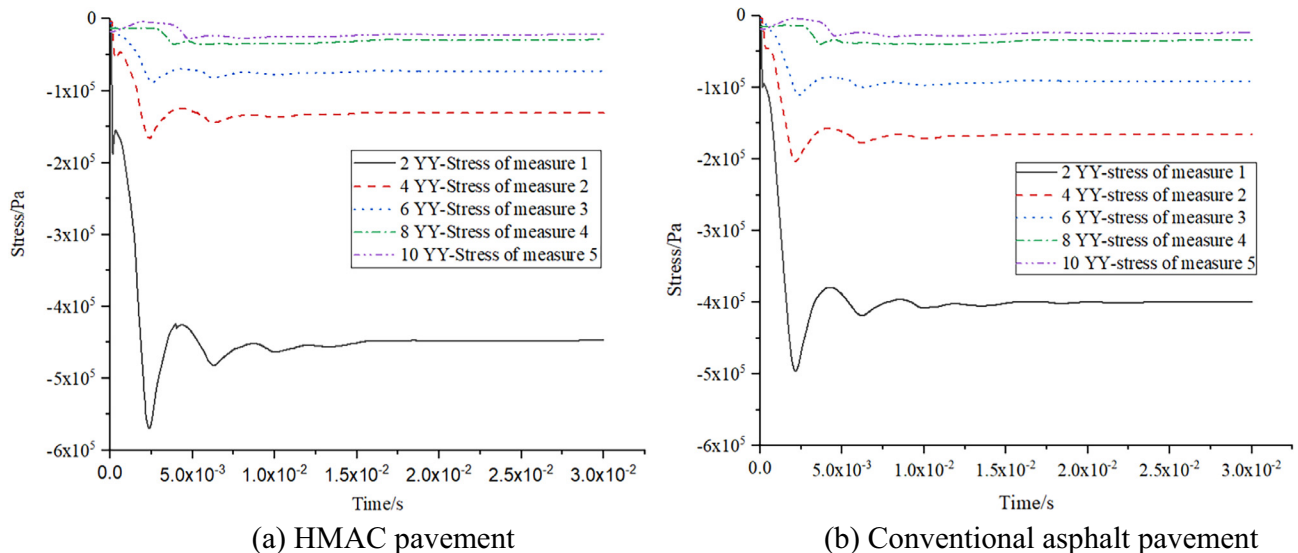
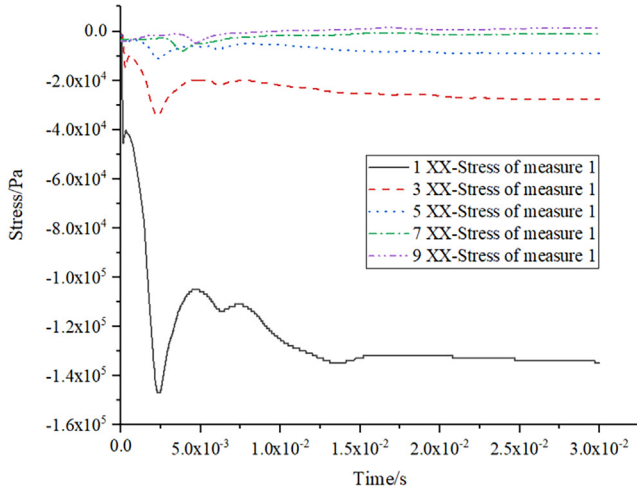


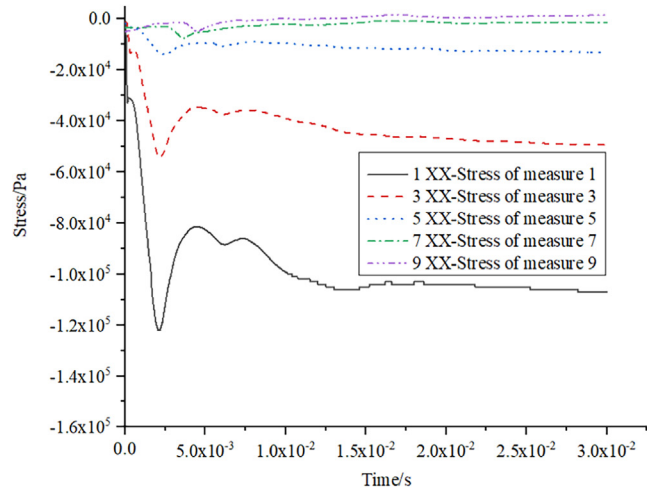
Fig. 13. Vertical stress distributions of two asphalt pavement structures at different depths beneath the left wheel load center.

Table 7
Comparison of vertical stresses at different depths below left wheel load center.

Depth/cm	4	10	18	53	75
Vertical stress of high modulus pavement structure (Pa)	-4.47×10^5	-1.31×10^5	-7.26×10^4	-2.89×10^4	-2.13×10^4
Vertical stress of conventional pavement structure (Pa)	-3.99×10^5	-1.66×10^5	-9.12×10^4	-3.36×10^4	-2.36×10^4



(a) HMAC pavement



(b) Conventional asphalt pavement

Fig. 14. Horizontal stress distribution of two asphalt pavement structures at different depths beneath the left wheel load center.

Table 8
Horizontal stresses at different depths below left wheel load center.

Depth/cm	4	10	18	53	75
Horizontal stress of high modulus pavement structure (Pa)	-1.35×10^5	-2.77×10^4	-9.16×10^3	-1.15×10^3	$+1.44 \times 10^3$
Horizontal stress of conventional pavement structure (Pa)	-1.07×10^5	-4.94×10^4	-1.3×10^4	-1.18×10^3	$+1.48 \times 10^3$

35.5 cm, 42.5 cm and 49.5 cm. For the subbase layer, measurement circles with a radius of 4.5 cm were horizontally arranged at depths of 57.5 cm, 66.5 cm, and 75.5 cm. continuing the previous numbering, the measurement circles were numbered as 6–45 from left to right, beginning at the top and proceeding to the bottom. The corresponding relationship between Measure ID and History ID is shown in Table 9.

The layout of the measurement circle is shown in Fig. 15.

For the HMAC pavement under the static load, the horizontal stress distributions at different depths and locations: at the outer edge of the wheel load ($x = -0.26625$ m), the center of the wheel load ($x = -0.15975$ m), the inner edge of the wheel load ($x = -0.05325$ m), and the center of the wheel gap ($x = 0.0$ m), are shown in Fig. 16 and Table 10.

As shown in Fig. 16 and Table 10, below the center of the wheel loading, the horizontal compressive stress presented in the surface layers and base layer gradually decreased with increasing depth. It was converted to be horizontal tensile stress at the subbase layer and increased with increasing depth.

In the bottom surface layer, the maximum horizontal compressive stress occurred at the wheel gap while the minimum horizontal

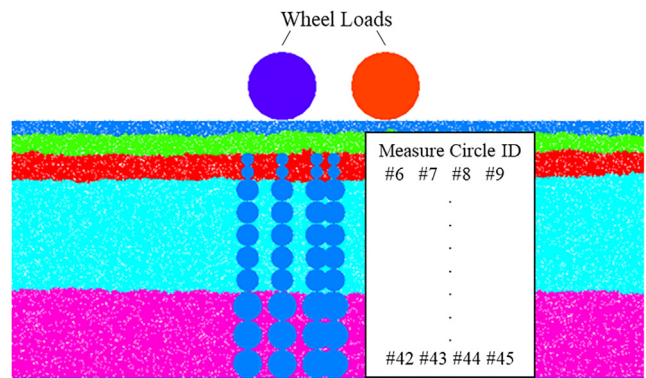


Fig. 15. The layout of the measurement circles.

pressure stress appeared at the loading center. In the subbase layer, the value and range of tensile stress were greater near the wheel gap in the horizontal direction. The maximum tensile stress

Table 9
The corresponding relationship between Measure ID and History ID.

Measure ID	6	7	8	9	10	...	37	38	39	40	41	42	43	44	45
History ID (stressxx)	11	12	13	14	15	...	42	43	44	45	46	47	48	49	50

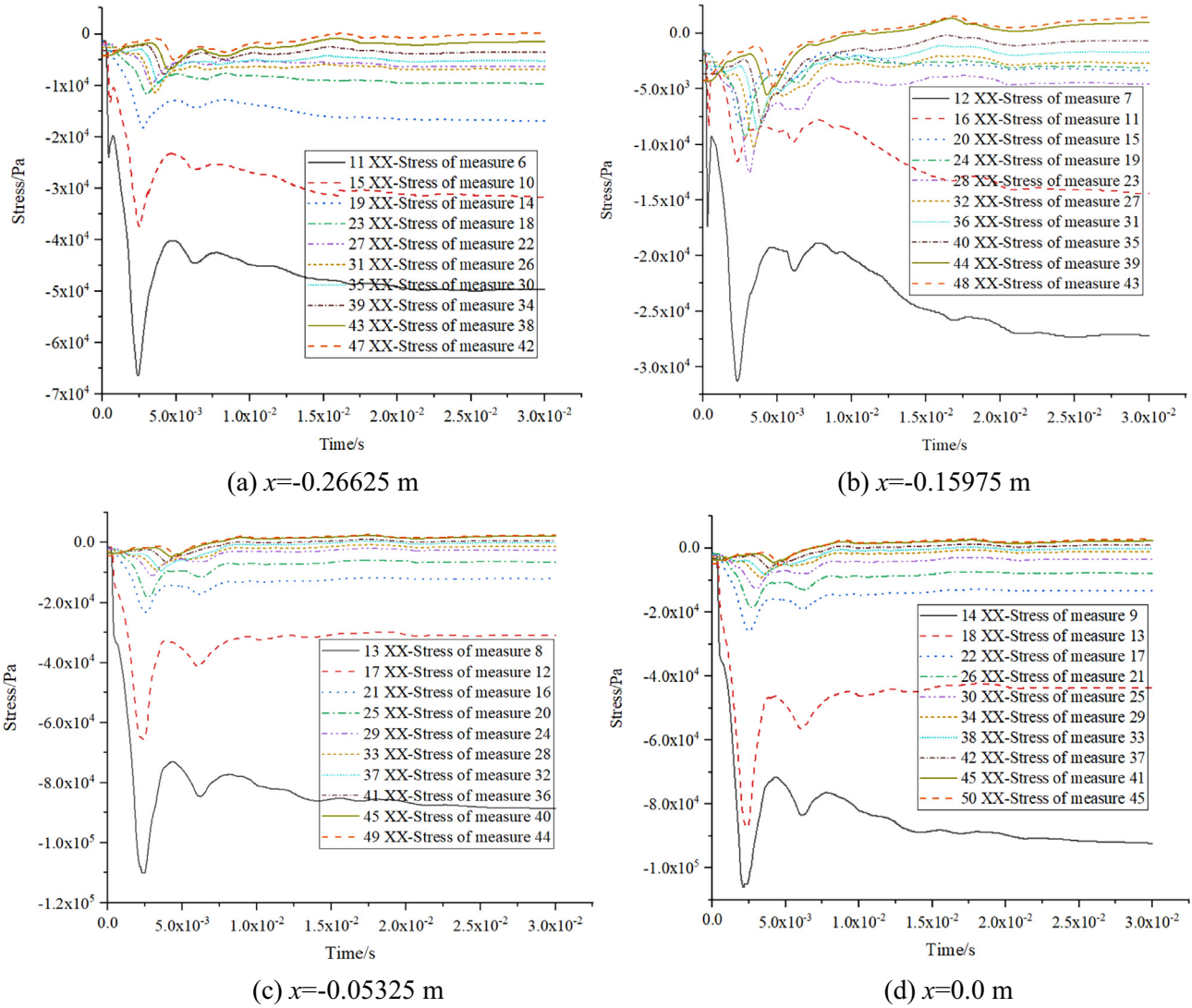


Fig. 16. Horizontal stress distribution at different depths and locations.

Table 10
Horizontal stress distribution of HMAC pavement Pa.

Depth (cm)	Location (m)			
	-0.266 25	-0.159 75	-0.053 25	0.0
12	-4.97×10^4	-2.72×10^4	-8.86×10^4	-9.22×10^4
16	-3.17×10^4	-1.44×10^4	-3.1×10^4	-4.36×10^4
21.5	-1.69×10^4	-3.36×10^3	-1.21×10^4	-1.32×10^4
28.5	-9.67×10^3	-3.09×10^3	-6.46×10^3	-7.78×10^3
35.5	-6.4×10^3	-4.54×10^3	-2.59×10^3	-3.51×10^3
42.5	-6.94×10^3	-2.7×10^3	-1.36×10^3	-1.12×10^3
49.5	-5.23×10^3	-1.7×10^3	-8.42×10^1	-1.05×10^2
57.5	-3.6×10^3	-6.32×10^2	6.72×10^2	9.81×10^2
66.5	-1.51×10^3	9.93×10^2	2.1×10^3	2.35×10^3
75.5	1.88×10^2	1.46×10^3	2.5×10^3	2.86×10^3

of the pavement structure appeared in the subbase layer with the value of 2.86×10^3 Pa.

For the conventional asphalt pavement under the static load, the horizontal stress distributions at different depths and locations: at the outer edge of the wheel load ($x = -0.26625$ m); the center of the wheel load ($x = -0.15975$ m); the inner edge of the wheel load ($x = -0.05325$ m); and the center of the wheel gap ($x = 0.0$ m), are shown in Fig. 17 and Table 11.

As shown in Fig. 17 and Table 11, tensile stress appeared in the base layer and subbase layer of conventional asphalt pavement, but there was no tensile stress in the base layer of the HMAC pavement. Therefore, the high modulus layer reduced the tensile stress, as a result, it improved the performance of the pavement, which was consistent with the conclusions of previous studies [22,23].

3.4. Horizontal shear stress

The horizontal shear stress ($stress_{xy}$) was calculated using measurement circles. Measurement circles with two radii were placed at different depths and locations in the surface layers. The locations included the outer edge of the wheel ($x = -0.26625$ m), the center of the wheel load ($x = -0.15975$ m), the inner edge of the wheel ($x = -0.05325$ m), and the center of the wheel gap ($x = 0.0$ m). Measurement circles with a radius of 2 cm were arranged horizontally at the depth of 4 cm, and measurement circles with a radius of 4 cm were arranged horizontally at depths of 10 cm and 18 cm. On the basis of previous numbering, measurement circles were numbered as 46–57 from left to right, beginning at the top and proceeding down. The corresponding relationship between Measure ID and History ID is shown in Table 12.

The layout of the measurement circle is shown in Fig. 18.

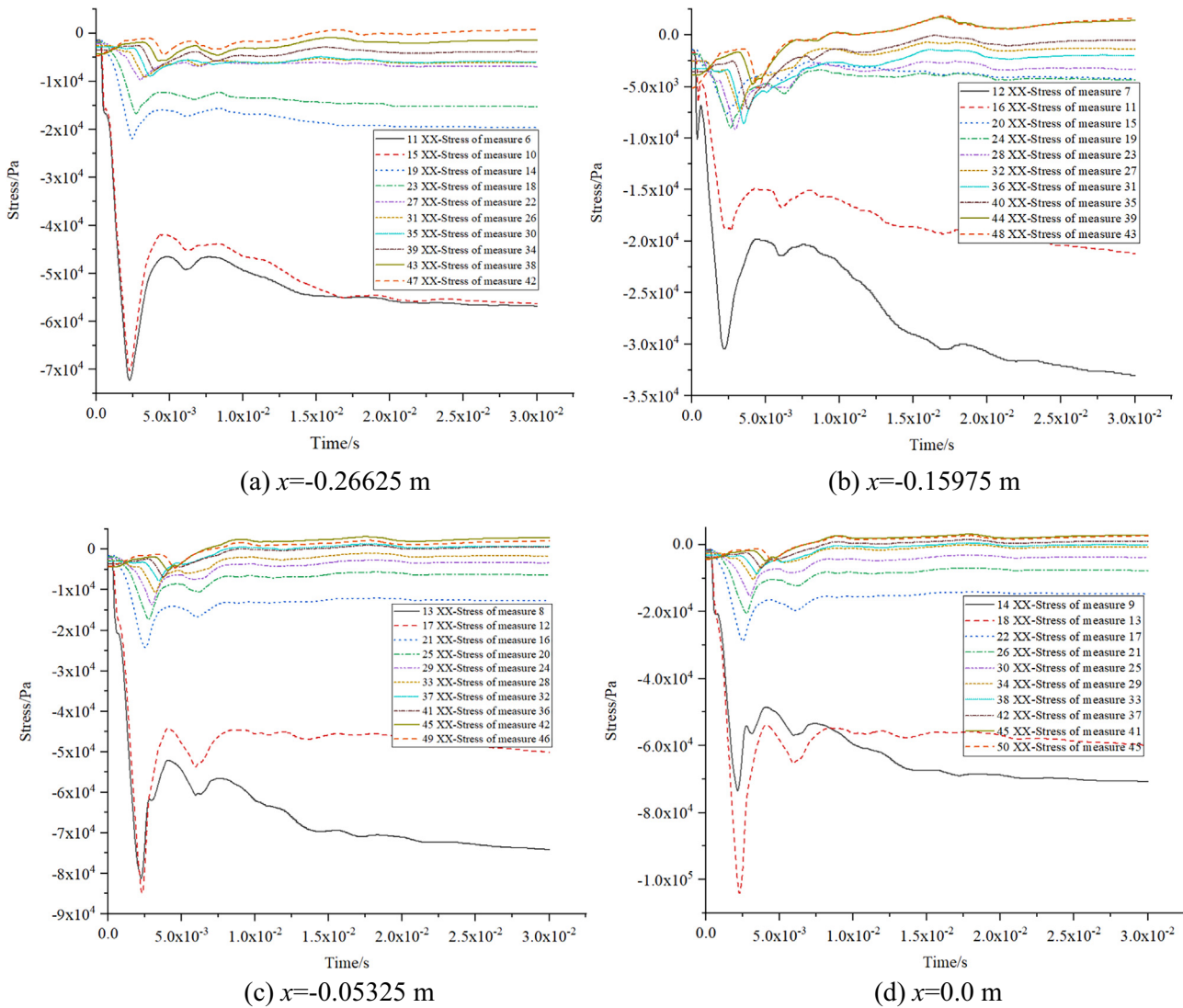


Fig. 17. Horizontal stress distribution at different depths and locations.

Table 11
Horizontal stress distribution of the conventional asphalt pavement (Pa).

Depth (cm)	Location (m)			
	-0.266 25	-0.159 75	-0.053 25	0.0
12	-5.68×10^4	-3.30×10^4	-7.41×10^4	-7.07×10^4
16	-5.63×10^4	-2.12×10^4	-5.01×10^4	-5.99×10^4
21.5	-1.97×10^4	-4.24×10^3	-1.27×10^4	-1.47×10^4
28.5	-1.53×10^4	-4.36×10^3	-6.33×10^3	-7.69×10^3
35.5	-6.92×10^3	-3.30×10^3	-3.31×10^3	-3.80×10^3
42.5	-6.15×10^3	-1.36×10^3	-1.64×10^3	-7.75×10^2
49.5	-5.94×10^3	-1.98×10^3	7.72×10^2	-6.84×10^1
57.5	-3.83×10^3	-5.11×10^2	6.35×10^2	1.04×10^3
66.5	-1.40×10^3	1.41×10^3	2.91×10^3	2.87×10^3
75.5	7.22×10^2	1.61×10^3	2.10×10^3	2.60×10^3

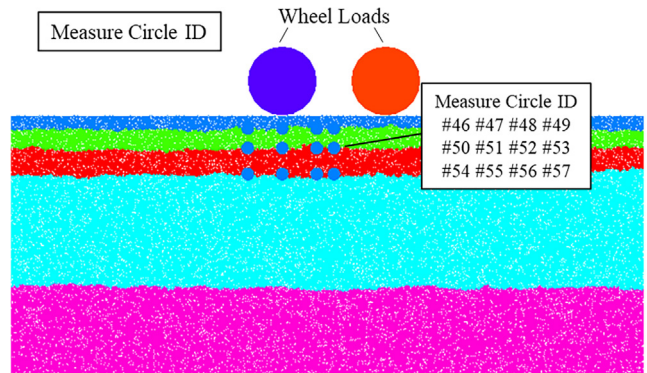


Fig. 18. The layout of the measurement circles.

Table 12
The corresponding relationship between Measure ID and History ID.

Measure ID	46	47	48	49	50	51	52	53	54	55	56	57
History ID (stressxy)	51	52	53	54	55	56	57	58	59	60	61	62

For the HMAC pavement under the static load, the horizontal shear stress distributions at the same depths and locations as previously mentioned: at the outer edge of the wheel load ($x = -0.26625$ m); the center of the wheel load ($x = -0.15975$ m); the inner edge of the wheel load ($x = -0.05325$ m); and the center of the wheel gap ($x = 0.0$ m), are shown in Fig. 19 and Table 13.

As shown in Fig. 19 and Table 13, the maximum horizontal shear stress (negative) existed underneath the outer edge of the wheel and the center of the wheel load, both appeared in the middle surface layer, which values were -5.85×10^5 Pa and -2.26×10^4 Pa, respectively. The maximum horizontal shear stress (positive) existed underneath the inner edge of the wheel appeared in the middle surface layer, the value was 2.5×10^4 Pa. The maximum horizontal shear stress underneath the center of the gap was positive, it occurred in the upper surface layer, and which value was 6.19×10^3 Pa. It showed that the maximum horizontal shear stress mainly occurred in the upper and middle surface layers. Under the action of shear stress, the pavement was likely to form rutting and embracing. Therefore, attention should be paid to improving the shear resistance of the surface layers during pavement design.

For the conventional asphalt pavement under the static load, the horizontal shear stress distribution at the outer edge of the

Table 13

Horizontal shear stress distribution of the HMAC pavement (Pa).

Depth (cm)	Location (m)			
	-0.266 25	-0.159 75	-0.053 25	0.0
4	-2.58×10^4	2.11×10^4	1.28×10^4	6.19×10^3
10	-5.85×10^4	-2.26×10^4	2.5×10^4	4.63×10^3
18	-2.88×10^4	-1.37×10^4	9.08×10^3	9.82×10^2

wheel load ($x = -0.26625$ m), the center of the wheel load ($x = -0.15975$ m), the inner edge of the wheel load ($x = -0.05325$ m), and the center of the wheel gap ($x = 0.0$ m), are shown in Fig. 20 and Table 14.

As shown in Fig. 20 and Table 14, the maximum horizontal shear stress (negative) existed underneath the outer edge of the wheel, which appeared on the middle surface layer, the value was -4.78×10^4 Pa. Underneath the center of the wheel load, the maximum horizontal shear stress (negative) occurred in the bottom surface layer, the value was -1.56×10^4 Pa. The maximum horizontal shear stress (positive) underneath the inner edge of the wheel appeared on the middle surface layer, the value was 2.36×10^4 Pa. The maximum horizontal shear stress underneath

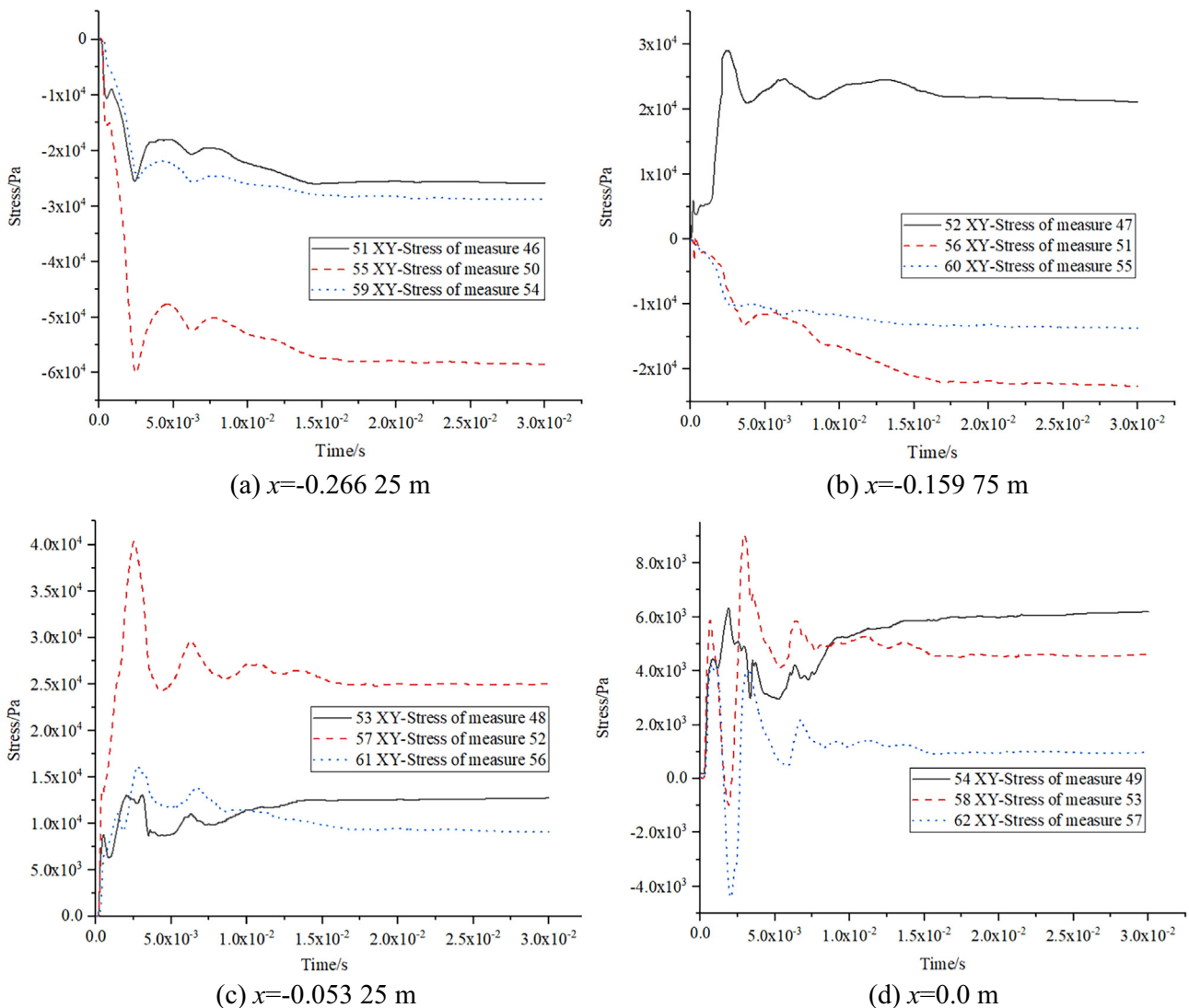


Fig. 19. Horizontal shear stress distribution at different depths and locations.

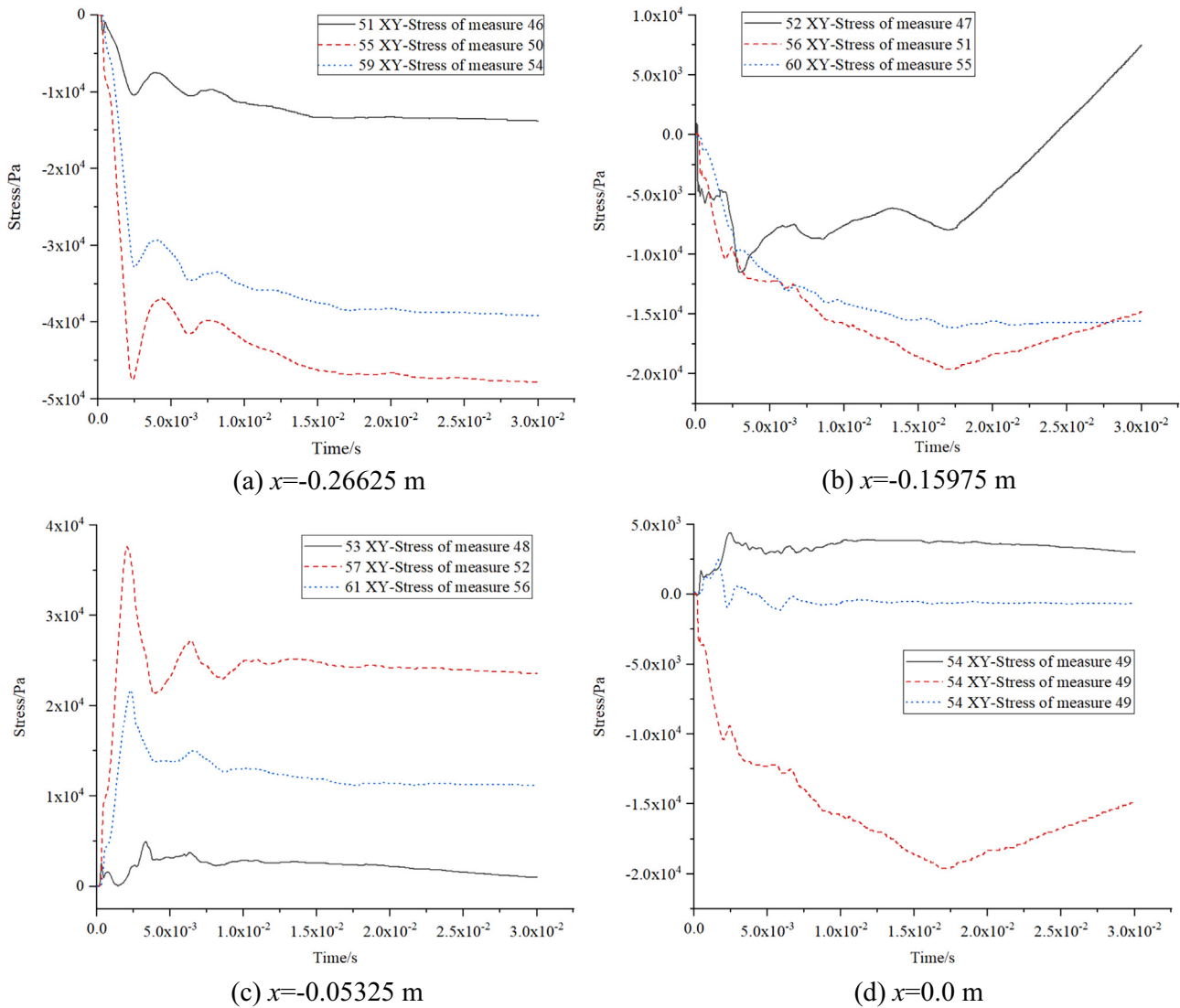


Fig. 20. Horizontal shear stress distribution at different depths and locations.

Table 14

Horizontal shear stress distribution of the conventional asphalt pavement (Pa).

Depth (cm)	Location (m)			
	-0.26625	-0.15975	-0.05325	0.0
4	-1.38×10^4	7.5×10^3	1.01×10^3	3.03×10^3
10	-4.78×10^4	-1.48×10^4	2.36×10^4	-2.53×10^3
18	-3.91×10^4	-1.56×10^4	1.12×10^4	-6.46×10^2

the center of the gap was positive and appeared in the upper surface layer, which value was 3.03×10^3 Pa.

By comparing the distribution of horizontal shear stress under static load between two types of pavement structures, it can be found that within the scope of the wheel load, $x = -0.26625 \sim -0.05325$ m, the horizontal shear stress of the HMAC pavement was slightly greater than the conventional asphalt pavement in the upper and middle surface layer while slightly less in the bottom surface layer. In cases where the high modulus layer exhibited a higher resistance to deformation, the HMAC pavement still had a lower potential of shear destruction compared to the conventional asphalt pavement.

4. Conclusions

In this study, the discrete element method (DEM) was used to establish the asphalt pavement structure models. The stress and displacement distribution of the two pavement structures under the static load were compared and analyzed. Based on the results of this study, the conclusions obtained were as follows:

1. In comparison to the conventional asphalt pavement, the HMAC pavement had a smaller vertical displacement than conventional asphalt pavement. Also, the high modulus layer effectively restrained the movement of the particles in the horizontal direction.
2. The application of high modulus materials decreased the vertical stress in the middle surface layer, while increase the vertical stress in the upper surface layer and decrease the vertical stress in the bottom surface layer.
3. The horizontal stress of the subbase layer of the HMAC pavement was smaller than that of the conventional asphalt pavement. The high modulus layer effectively reduced the horizontal tensile stress of pavement structure and improved the bending and rutting resistance.

Declaration of Competing Interest

None.

Acknowledgments

This work was supported by the National Natural Science Foundation of China (No. 11202142, 11302138), Principal Project of Hebei Province Department of Transportation (No. Y-2010021, No 2013-2-5), Youth Talent Support Program of Hebei Province and Distinguished Young Scientists Foundation of Hebei Provincial Education Department (YQ2014038).

References

- [1] J.-F. Corté, Development and uses of hard-grade asphalt and of high-modulus asphalt mixes in France, *Transport. Res. Circ.* 503 (2001) 12–31.
- [2] S.D. Capitão, L. Picado-Santos, Assessing permanent deformation resistance of high modulus asphalt mixtures, *J. Transp. Eng.* 132 (5) (2006) 394–401.
- [3] F. Moreno-Navarro et al., The use of additives for the improvement of the mechanical behavior of high modulus asphalt mixes, *Constr. Build. Mater.* 70 (2014) 65–70.
- [4] R. Zhang et al., High temperature performance of SBS modified bio-asphalt, *Constr. Build. Mater.* 144 (2017) 99–105.
- [5] H.J. Lee, J.H. Lee, H.M. Park, Performance evaluation of high modulus asphalt mixtures for long life asphalt pavements, *Constr. Build. Mater.* 21 (5) (2007) 1079–1087.
- [6] X. Wang et al., Study on durability of high-modulus asphalt mixture based on TLA and fibre composite modification technology, *Int. J. Pavement Eng.* 19 (10) (2018) 930–936.
- [7] T. Ma et al., Laboratory performance characteristics of high modulus asphalt mixture with high-content RAP, *Constr. Build. Mater.* 101 (2015) 975–982.
- [8] D. Rys et al., Comparison of low-temperature cracks intensity on pavements with high modulus asphalt concrete and conventional asphalt concrete bases, *Constr. Build. Mater.* 147 (2017) 478–487.
- [9] R. Miró et al., Evaluation of high modulus mixture behaviour with high reclaimed asphalt pavement (RAP) percentages for sustainable road construction, *Construct. Build. Mater.* 25 (10) (2011) 3854–3862.
- [10] M. Zheng et al., Simulation of permanent deformation in high-modulus asphalt pavement with sloped and horizontally curved alignment, *Appl. Sci.* 7 (4) (2017) 331.
- [11] M. Zheng et al., Fatigue life prediction of high modulus asphalt concrete based on the local stress-strain method, *Appl. Sci.* 7 (3) (2017) 305.
- [12] E. Masad et al., Characterization of air void distribution in asphalt mixes using X-ray computed tomography, *J. Mater. Civ. Eng.* 14 (2) (2002) 122–129.
- [13] M.N. Partl, A. Flisch, M. Jönsson, Comparison of laboratory compaction methods using x-ray computer tomography, *Road Mater. Pavement Design* 8 (2) (2007) 139–164.
- [14] H. Huang, E. Tutumluer, Image-aided element shape generation method in discrete-element modeling for railroad ballast, *J. Mater. Civ. Eng.* 26 (3) (2013) 527–535.
- [15] S. Kose et al., Distribution of strains within hot-mix asphalt binders: applying imaging and finite-element techniques, *Transport. Res. Rec. J. Transport. Res. Board* 1728 (2000) 21–27.
- [16] H. Wang et al., Characterising the asphalt concrete fracture performance from X-ray CT Imaging and finite element modelling, *Int. J. Pavement Eng.* 19 (3) (2018) 307–318.
- [17] L. You, Z. You, K. Yan, Effect of anisotropic characteristics on the mechanical behavior of asphalt concrete overlay, *Front. Struct. Civil Eng.* 13 (1) (2019) 110–122.
- [18] K.-N.G. Chang, J.N. Meegoda, Micromechanical simulation of hot mix asphalt, *J. Eng. Mech.* 123 (5) (1997) 495–503.
- [19] Z. You, W.G. Buttlar, Application of discrete element modeling techniques to predict the complex modulus of asphalt–aggregate hollow cylinders subjected to internal pressure, *Transp. Res. Rec.* 1929 (1) (2005) 218–226.
- [20] W. Buttlar, Z. You, Discrete element modeling of asphalt concrete: microfabric approach, *Transport. Res. Rec. J. Transport. Res. Board* 1757 (2001) 111–118.
- [21] H. Kim, W.G. Buttlar, Micromechanical fracture modeling of asphalt mixture using the discrete element method, *Adv. Pavement Eng.* (2005) 1–15.
- [22] A. Abbas et al., Micromechanical modeling of the viscoelastic behavior of asphalt mixtures using the discrete-element method, *Int. J. Geomech.* 7 (2) (2007) 131–139.
- [23] J. Chen et al., Application of discrete element method to Superpave gyratory compaction, *Road Mat. Pavement Design* 13 (3) (2012) 480–500.
- [24] Y. Liu et al., Discrete element modeling of realistic particle shapes in stone-based mixtures through MATLAB-based imaging process, *Constr. Build. Mater.* 143 (Suppl. C) (2017) 169–178.
- [25] F. Gong et al., Lab assessment and discrete element modeling of asphalt mixture during compaction with elongated and flat coarse aggregates, *Constr. Build. Mater.* 182 (2018) 573–579.
- [26] Liu, Y., et al., Determining aggregate grain size using discrete–element models of sieve analysis, 2019, 19, 4, p. 04019014.
- [27] D.O. Potyondy, The bonded-particle model as a tool for rock mechanics research and application: current trends and future directions, *Geosystem Eng.* 18 (1) (2015) 1–28.
- [28] Y. Peng, J.-X. Bao, Comparative study of 2D and 3D micromechanical discrete element modeling of indirect tensile tests for asphalt mixtures, *Int. J. Geomech.* 18 (6) (2018) 04018046.
- [29] Y. Liu, Q. Dai, Z. You, Viscoelastic model for discrete element simulation of asphalt mixtures, *J. Eng. Mech.* 135 (4) (2009) 324–333.
- [30] W. Cai et al., Discrete element modelling of creep of asphalt mixtures, *Geomech. Geoeng.* 11 (1) (2016) 64–72.
- [31] H. Kim, M.P. Wagoner, W.G. Buttlar, Numerical fracture analysis on the specimen size dependency of asphalt concrete using a cohesive softening model, *Constr. Build. Mater.* 23 (5) (2009) 2112–2120.
- [32] H.-C. Dan et al., Numerical simulation of an indirect tensile test for asphalt mixtures using discrete element method software, *J. Mater. Civ. Eng.* 30 (5) (2018) 04018067.
- [33] Y. Liu, Z. You, Visualization and simulation of asphalt concrete with randomly generated three-dimensional models, *J. Comput. Civil Eng.* 23 (6) (2009) 340–347.
- [34] Y. Liu, Z. You, Discrete-element modeling: impacts of aggregate sphericity, orientation, and angularity on creep stiffness of idealized asphalt mixtures, *J. Eng. Mech.* 137 (4) (2011) 294–303.